

Time-domain Raman analytical forward solvers

FABRIZIO MARTELLI,^{1,*} TIZIANO BINZONI,^{2,3} SANATHANA KONUGOLU VENKATA SEKAR,⁴ ANDREA FARINA,⁵ STEFANO CAVALIERI,¹ AND ANTONIO PIFFERI⁴

¹Università degli Studi di Firenze, Dipartimento di Fisica e Astronomia, Via G. Sansone 1, 50019 Sesto Fiorentino, Firenze, Italy

²Département de Neurosciences Fondamentales, University of Geneva, Switzerland

³Département de l'Imagerie et des Sciences de l'Information Médicale, University Hospital, Geneva, Switzerland

⁴Dipartimento di Fisica, Politecnico di Milano, Milano, Italy, Piazza Leonardo da Vinci 32, 20133 Milano, Italy

⁵Istituto di Fotonica e Nanotecnologie, Consiglio Nazionale delle Ricerche, Piazza Leonardo da Vinci 32, 20133 Milano, Italy

*fabrizio.martelli@unifi.it

Abstract: A set of time-domain analytical forward solvers for Raman signals detected from homogeneous diffusive media is presented. The time-domain solvers have been developed for two geometries: the parallelepiped and the finite cylinder. The potential presence of a background fluorescence emission, contaminating the Raman signal, has also been taken into account. All the solvers have been obtained as solutions of the time dependent diffusion equation. The validation of the solvers has been performed by means of comparisons with the results of “gold standard” Monte Carlo simulations. These forward solvers provide an accurate tool to explore the information content encoded in the time-resolved Raman measurements.

© 2016 Optical Society of America

OCIS codes: (300.6450) Spectroscopy, Raman; (170.5660) Raman spectroscopy; (170.3660) Light propagation in tissues; (170.5280) Photon migration; (170.6280) Spectroscopy, fluorescence and luminescence.

References and links

1. P. Matousek and M. D. Morris, *Emerging Raman Applications and Techniques in Biomedical and Pharmaceutical Fields* (Springer, 2010).
2. C. A. Froud, I. P. Hayward, and J. Laven, “Advances in the Raman Depth Profiling of Polymer Laminates,” *Appl. Spectrosc.* **57**(12), 1468–1474 (2003).
3. N. J. Everall, “Confocal Raman microscopy: common errors and artefacts,” *Analyst* **135**(10), 2512–2522 (2010).
4. P. Matousek, and N. Stone, “Recent advances in the development of Raman spectroscopy for deep non-invasive medical diagnosis,” *J. Biophotonics* **1**(5), 7–19 (2013).
5. K. Sowidnich, J. H. Churchwell, K. Buckley, A. E. Goodship, A. W. Parker, and P. Matousek, “Photon migration of Raman signal in bone as measured with spatially offset Raman spectroscopy,” *J. Raman Spectrosc.* **47**(2), 240–247 (2015).
6. P. Matousek, I. P. Clark, E. R. C. Draper, M. D. Morris, A. E. Goodship, N. Everall, M. Towrie, W. F. Finney, and A. W. Parker, “Subsurface Probing in Diffusely Scattering Media Using Spatially Offset Raman Spectroscopy,” *Appl. Spectrosc.* **59**(4), 393–400 (2005).
7. N. Stone, R. Baker, K. Rogers, A. W. Parker, and P. Matousek, “Subsurface probing of calcifications with spatially offset Raman spectroscopy (SORS): future possibilities for the diagnosis of breast cancer,” *Analyst* **132**(9), 899–905 (2007).
8. P. Matousek, E. R. C. Draper, A. E. Goodship, I. P. Clark, K. L. Ronayne, and A. W. Parker, “Noninvasive Raman Spectroscopy of Human Tissue In Vivo,” *Appl. Spectrosc.* **60**(7), 758–763 (2006).
9. W. J. Olds, E. Jaatinen, P. Fredericks, B. Cletus, H. Panayiotou, and E. L. Izake, “Spatially offset Raman spectroscopy (SORS) for the analysis and detection of packaged pharmaceuticals and concealed drugs,” *Forensic Sci. Int.* **212**(1-3), 69–77 (2011).
10. D. Yang and Y. Ying, “Applications of Raman Spectroscopy in Agricultural Products and Food Analysis: A Review,” *Appl. Spectrosc. Rev.* **46**(7), 539–560 (2011).
11. C. Conti, C. Colombo, M. Realini, and P. Matousek, “Subsurface analysis of painted sculptures and plasters using micrometre-scale spatially offset Raman spectroscopy (micro-SORS),” *J. Raman Spectrosc.* **46**(5), 476–482 (2015).
12. J. Johansson, S. Pettersson, and S. Folestad, “Characterization of different laser irradiation methods for quantitative Raman tablet assessment,” *J. Pharm. Biomed. Anal.* **39**(3-4), 510–516 (2005).

13. P. Matousek and A. W. Parker, "Bulk Raman Analysis of Pharmaceutical Tablets," *Appl. Spectrosc.* **60**(12), 1353–1357 (2006).
14. M. V. Schulmerich, J. H. Cole, K. A. Dooley, M. D. Morris, J. M. Kreider, S. A. Goldstein, S. Srinivasan, and B. W. Pogue, "Noninvasive Raman tomographic imaging of canine bone tissue," *J. Biomed. Opt.* **13**(2), 020506 (2008).
15. J.-L. H. Demers, S. C. Davis, B. W. Pogue, and M. D. Morris, "Multichannel diffuse optical Raman tomography for bone characterization in vivo: a phantom study," *Biomed. Opt. Express* **3**(9), 2299–2305 (2012).
16. J.-L. H. Demers, F. W. L. Esmonde-White, K. A. Esmonde-White, M. D. Morris, and B. W. Pogue, "Next-generation Raman tomography instrument for non-invasive in vivo bone imaging," *Biomed. Opt. Express* **6**(3), 793–806 (2015).
17. J. Steinbrink, H. Wabnitz, H. Obrig, A. Villringer, and H. Rinneberg, "Determining changes in NIR absorption using a layered model of the human head," *Phys. Med. Biol.* **46**(3), 879–896 (2001).
18. P. Matousek, M. Towrie, A. Stanley, and A. W. Parker, "Efficient Rejection of Fluorescence from Raman Spectra Using Picosecond Kerr Gating," *Appl. Spectrosc.* **53**(12), 1485–1489 (1999).
19. J. Wu, Y. Wang, L. Perelman, I. Itzkan, R. R. Dasari, and M. S. Feld, "Three-dimensional imaging of objects embedded in turbid media with fluorescence and Raman spectroscopy," *Appl. Opt.* **34**(18), 3425–3430 (1995).
20. P. Matousek, N. Everall, M. Towrie, and A. W. Parker, "Depth profiling in diffusely scattering media using Raman spectroscopy and picosecond Kerr gating," *Appl. Spectrosc.* **59**(2), 200–205 (2005).
21. F. Ariese, H. Meuzelaar, M. M. Kerssens, J. B. Buijs, and C. Gooijer, "Picosecond Raman spectroscopy with a fast intensified CCD camera for depth analysis of diffusely scattering media," *Analyst* **134**(6), 1192–1197 (2009).
22. S. Sundarajoo, E.L. Izake, W. Olds, B. Cletus, E. Jaatinen, and P. M. Fredericks, "Non-invasive depth profiling by space and time-resolved Raman spectroscopy," *J. Raman Spectr.* **44**(7), 949–956 (2013).
23. E. L. Izake, B. Cletus, W. Olds, S. Sundarajoo, P. M. Fredericks, and E. Jaatinen, "Deep Raman spectroscopy for the non-invasive standoff detection of concealed chemical threat agents," *Talanta* **94**, 342–347 (2012).
24. A. Dalla Mora, E. Martinenghi, D. Contini, A. Tosi, G. Boso, T. Durduran, S. Arridge, F. Martelli, A. Farina, A. Torricelli, and A. Pifferi, "Fast silicon photomultiplier improves signal harvesting and reduces complexity in time-domain diffuse optics," *Opt. Express* **23**(11), 13937–13946 (2015).
25. A. Dalla Mora, D. Contini, S. Arridge, F. Martelli, A. Tosi, G. Boso, A. Farina, T. Durduran, E. Martinenghi, A. Torricelli, and A. Pifferi, "Towards next-generation time-domain diffuse optics for extreme depth penetration and sensitivity," *Biomed. Opt. Express* **6**(5), 1749–1760 (2015).
26. F. Martelli, T. Binzoni, A. Pifferi, L. Spinelli, A. Farina, and A. Torricelli, "There's plenty of light at the bottom: statistics of photon penetration depth in random media," *Sci. Rep.* **6**, 27057 (2016).
27. D. Contini, F. Martelli, and G. Zaccanti, "Photon migration through a turbid slab described by a model based on diffusion approximation. I. Theory," *Appl. Opt.* **36**(19), 4588–4599 (1997).
28. F. Martelli, S. Del Bianco, A. Ismaelli, and G. Zaccanti, *Light Propagation through Biological Tissue and Other Diffusive Media: Theory, Solutions and Software* (SPIE, 2010).
29. N. Everall, T. Hahn, P. Matousek, A. W. Parker, and M. Towrie, "Photon Migration in Raman Spectroscopy," *Appl. Spect.* **58**(5), 591–597 (2004).
30. R. A. Desiderio, "Application of the Raman scattering coefficient of water to calculations in marine optics," *Appl. Opt.* **39**(12), 1893–1894 (2000).
31. A. Bray, R. Chapman R, and T. Plakhotnik, "Accurate measurements of the Raman scattering coefficient and the depolarization ratio in liquid water," *Appl. Opt.* **52**(11), 2503–2510 (2013).
32. N. Everall, T. Hahn, P. Matousek, A. W. Parker, and M. Towrie, "Picosecond Time-Resolved Raman Spectroscopy of Solids: Capabilities and Limitations for Fluorescence Rejection and the Influence of Diffuse Reflectance," *Appl. Spect.* **55**(12), 1701–1708 (2001).
33. H. S. Carslaw, and J. C. Jaeger, *Conduction of Heat in Solids* (Oxford University, 1959).
34. J. Wu, Y. Wang, L. Perelman, I. Itzkan, R. R. Dasari, and M. S. Feld, "Three-dimensional imaging of objects embedded in turbid media with fluorescence and Raman spectroscopy," *Appl. Spect.* **34**(18), 3425–3430 (1995).
35. A. Sassaroli, and F. Martelli, "Equivalence of four Monte Carlo methods for photon migration in turbid media," *J. Opt. Soc. Am. A* **29**(10), 2110–2117 (2012).
36. E. Alerstam, T. Svensson, and S. Andersson-Engels, "Parallel computing with graphics processing units for high-speed Monte Carlo simulation of photon migration," *J. Biomed. Opt.* **13**(6), 060504 (2008).

1. Introduction

Due to its excellent chemical specificity, Raman spectroscopy has been largely investigated in biomedical diagnosis and industrial applications [1]. In most cases, a quasi-confocal approach was adopted, which limits the investigated volume to a maximum depth $< 200 \mu\text{m}$ [2, 3]. For this reason, in the last decade, much interest was raised on the possibility to detect Raman signals well beneath the surface [4]. The most popular approach was named Spatially Offset Raman Spectroscopy (SORS). SORS exploits the detection of Raman signals at increasing distances from the laser injection point to discriminate structures at different depth [4–6]. Based on SORS, many applications have been proposed with huge industrial impact. Applications range

from medical diagnostics (e.g. detection of cancer [7] or bone pathologies [8]), to security and forensic applications (e.g. identification of liquids or solids through plastic or glass containers [9]), and also to non-destructive food assessment [10] or analysis of paintings [11]. Another approach was adopted for the analysis of pharmaceutical tablets, by exploiting a transmittance geometry [12, 13]. Similar concepts have also permitted to obtain tomographic Raman images through tissue simulating phantoms, biological specimens and, *in vivo*, on animals [14–16].

All approaches mentioned above are based on continuous wave (CW) illumination. A further different option is the adoption of a time-resolved (TR) injection and detection scheme. The TR scheme exploits the property that the more diffused photons are detected later on in time, the more they have penetrated deeply into the medium [17]. A further advantage of this method is that the use of a time-gated scheme permits to reject a significant fraction of the contaminating fluorescence emission [18]. The experimental feasibility of deep Raman spectroscopy using the TR approach was demonstrated using time-correlated single-photon counting [19], ultrafast (ps) Kerr-Gate spectroscopy [20] and fast gated camera [21–23].

It is important to note that the TR research direction, although possibly more informative than SORS, has to face with the complexity of the TR systems, which has hampered until nowadays a more widespread use. However, even if the translation of these methods and devices to Raman spectroscopy is not straightforward, a dramatic reduction of TR system complexity is expected by the use of novel compact photonics devices like Silicon Photomultipliers (SIPMs) [24]. Thus, TR systems could definitely increase their impact in the near future because of the great potentialities offered by this instrumentation to gain depth information [25, 26].

In this framework, the development of rigorous mathematical algorithms, constituting one of the core elements of the TR systems, appears to be a fundamental issue. Moreover, theoretical models may also serve as a support for simulation studies in the development of novel measurement schemes, or in the understanding of the physics of Raman signal from its generation to its propagation and detection. For this reason, in the present work we address the rigorous modeling of TR diffused Raman based on the diffusion approximation (DA) to the Radiative Transfer Equation (RTE).

In summary, in the time domain exact analytical models describing propagation of Raman signals in diffusive media are still lacking. With the present work, we want to provide a general perspective of time domain diffuse Raman spectroscopy through its possible information content in terms of sensitiveness to the optical properties of the medium. We have developed a set of forward analytical solvers describing the TR Raman reflectance for a parallelepiped and a finite cylinder. The solvers have been obtained exploiting the DA to the RTE [27, 28] and the Green's function theorem [28], and they have been systematically validated by “gold standard” Monte Carlo (MC) simulations for a wide set of physical conditions. Finally, the range of validity of an often used simplified heuristic model [6] for time-domain Raman signal is also discussed.

2. Theory and methods

In this section, we review the theory of Raman scattering within the framework of the diffusion equation (DE) and we obtain analytical solutions for the Raman TR reflectance. The analytical theory is also developed for a background medium hosting distributed fluorescent molecules. The MC method used to generate “gold standard” data for the whole study is also presented.

2.1. Preamble

The origin of Raman scattering [1, 4, 29] is quite different from the classical Tyndall scattering. Tyndall scattering depends on the micro-structures of materials and on their heterogeneities, while Raman scattering depends on the intrinsic properties of molecules. Further, Tyndall scattering is an elastic interaction, only affecting the direction of photon migration, while Raman scattering is an inelastic phenomenon affecting direction and wavelength of the re-emitted pho-

ton. This means that the two phenomena are characterized by independent scattering coefficients, but, more relevant, it also implies that a couple of independent RTEs need to be introduced for dealing with two different wavelengths λ and λ_e . Raman scattering can be considered “equivalent” to an absorption interaction since the scattered photon is no longer available at the excitation wavelength, and thus can be accounted as a loss factor in the energy balance at this wavelength. We follow this approach in developing the analytical theory here described.

Figure 1 shows the excitation light at λ (isotropic point source at \mathbf{r}_s), and the Raman light at λ_e , which is emitted from a scatter at \mathbf{r}' and collected at point \mathbf{r} . The global, absorption and scattering coefficients of the medium originate from: 1) the background medium and; 2) the Raman scattering molecules. The Raman signal is affected by Tyndall multiple scattering in the background at both excitation, λ , and emission, λ_e , wavelengths. The global optical parameters: absorption coefficient, scattering coefficient, reduced scattering coefficient, and the refractive index of the investigated medium at λ are denoted, respectively, as μ_a , μ_s , μ'_s , and n_i , and at λ_e as μ_{ae} , μ_{se} , μ'_{se} , and n_{ie} . For the background medium the absorption coefficient, the scattering coefficient, and the reduced scattering coefficient at λ are denoted, respectively, as μ_{ab} , μ_{sb} , μ'_{sb} , and at λ_e as μ_{abe} , μ_{sbe} , μ'_{sbe} . We assume that Raman scattering molecules are distributed inside the whole volume of the medium with scattering coefficient μ_{sR} at λ , and μ_{sRe} at λ_e . We also assume that $\mu_{sRe} = 0$, excluding the possibility of a second Raman scattering event on the same photon [4] (see next section). Being Raman interactions described by a scattering coefficient, their effects at λ , at least within the DE, can only be modeled with an equivalent effective “absorption” term. Thus, since Raman scattering at λ determines an instantaneous re-emission of light at λ_e , for the purpose of the energy balance at λ , Raman interactions are equivalent to absorption events, and therefore, we can then write $\mu_a = \mu_{ab} + \mu_{sR}$, $\mu_s = \mu_{sb}$ and $\mu'_s = \mu'_{sb}$. For a summary of the notation used see the column denoted Raman in Table 1. This approach may appear to be not orthodox from a physical point of view, but, what it really matters is to perform a correct energy balance at λ and λ_e , without neglecting terms influencing the photon migration. In the next sections the validity of the proposed modeling of Raman scattering will be further discussed and demonstrated by means of MC simulations.

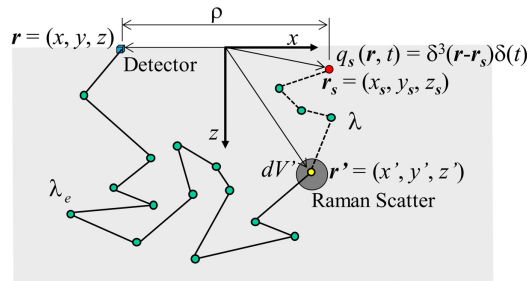


Fig. 1. Diagram of a photon path trajectory in a x, z plane projection from the source (red circle) to the Raman scatter (dashed line) and from the Raman scatter to the detector (continuous line). Green circles are Tyndall interactions. The yellow circle is a Raman interaction.

2.2. General Raman model based on the time-dependent diffusion equation

Light propagation through biological tissues and other highly scattering media can be described with the time-dependent DE [27, 28] due to the diffusive regime of propagation that is often established in these media. Therefore, the Raman signal can be described by two coupled diffusion

equations for the time-dependent photon fluence rate, $\Phi(\mathbf{r}, t)$ and $\Phi_e(\mathbf{r}, t)$, at λ and λ_e :

$$\left[\frac{1}{v} \frac{\partial}{\partial t} + \mu_a - D \nabla^2 \right] \Phi(\mathbf{r}, t) = q(\mathbf{r}, t), \quad (1)$$

$$\left[\frac{1}{v_e} \frac{\partial}{\partial t} + \mu_{ae} - D_e \nabla^2 \right] \Phi_e(\mathbf{r}, t) = q_e(\mathbf{r}, t), \quad (2)$$

where $D = 1/(3\mu'_s)$ and $D_e = 1/(3\mu'_{se})$ are the diffusion coefficients at λ and λ_e and v and v_e are the speed of light in the medium at λ and λ_e . The term $q(\mathbf{r}, t)$ is the real source term at λ , while $q_e(\mathbf{r}, t)$ represents the virtual source term, at λ_e , generated by Raman scatterers. To facilitate the reading, the dependence of $\Phi(\cdot)$ and $\Phi_e(\cdot)$ on variables other than \mathbf{r} and t will be explicitly written along the manuscript only when necessary.

Equations (1) and (2) are coupled by the physical relationship existing between the excitation fluence rate, $\Phi(\mathbf{r}, t)$, and the source term $q_e(\mathbf{r}, t)$. As we have highlighted above, at λ the effect of Raman scattering is “equivalent” to an “absorption” interaction. Then, μ_{sR} can be accounted in Eq. (1) as an absorption term so that $\mu_a = \mu_{ab} + \mu_{sR}$. The source term $q_e(\mathbf{r}, t)$, at λ_e , accounts for the number of photons generated at this wavelength per unit volume and time due to Raman scattering events at λ . Thus, using the fluence rate at λ , $\Phi(\mathbf{r}_s, \mathbf{r}', \mu_a, \mu'_s, n_i, t', \lambda)$, the source term can be written as

$$q_e(\mathbf{r}', t', \lambda_e) = \mu_{sR} \Phi(\mathbf{r}_s, \mathbf{r}', \mu_a, \mu'_s, n_i, t', \lambda). \quad (3)$$

Assuming an isotropic source term of unitary strength $q(\mathbf{r}, t) = \delta^3(\mathbf{r} - \mathbf{r}_s) \delta(t)$, then Φ in Eq. (3) is the Green's function, G , of the problem and q_e can be written as

$$q_e(\mathbf{r}', t', \lambda_e) = \mu_{sR} G(\mathbf{r}_s, \mathbf{r}', \mu_a, \mu'_s, n_i, t', \lambda). \quad (4)$$

By substituting Eq. (4) in Eq. (2), the following equation at λ_e is obtained:

$$\left[\frac{1}{v_e} \frac{\partial}{\partial t} + \mu_{ae} - D_e \nabla^2 \right] \Phi_e(\mathbf{r}, t) - \mu_{sR} G(\mathbf{r}_s, \mathbf{r}, t) = 0. \quad (5)$$

According to the Green's function theorem [28], the fluence rate at λ_e , $\Phi_e(\mathbf{r}, t)$, due to the Raman scattering at λ is given by

$$\Phi_e(\mathbf{r}, t) = \int_0^t \int_{V'} q_e(\mathbf{r}', t') G_e(\mathbf{r}', \mathbf{r}, \mu_{ae}, \mu'_{se}, n_{ie}, t - t') dV' dt', \quad (6)$$

with G_e the Green's function at λ_e . We stress that the Green's functions G and G_e are related to the same medium, so that the different notation is maintained only to keep the distinction between λ and λ_e . Putting all explicitly,

$$\Phi_e(\mathbf{r}, t) = \mu_{sR} \int_0^t \int_{V'} G(\mathbf{r}_s, \mathbf{r}', \mu_a, \mu'_s, n_i, t') G_e(\mathbf{r}', \mathbf{r}, \mu_{ae}, \mu'_{se}, n_{ie}, t - t') dV' dt'. \quad (7)$$

Equation (7) is the convolution in time of G with the same Green's function calculated at the site of the Raman scatterers.

We remind that Eq. (7) is obtained under the assumption that only single scattering Raman events contribute to the solution. In principle, also multiple scattering Raman events can be possible. But, given the low values for the probability of Raman scattering (usually less than 10^{-6}) [30, 31], their contribution to the calculation can be considered negligible. Moreover, in Eq. (7) it is implicitly assumed that the angular re-emission of Raman scattering is the same of Tyndall scattering since no distinctions on this point are made in the theory. Starting from

Eq. (7) it is possible to derive the solution of the Raman signal for any desired geometry. In particular, Raman scatters can be homogeneously distributed inside the medium, but they can also occupy a small portion of the whole medium resulting as an inclusion. In this work we focus our analysis on geometries where the Raman scatters are homogeneously distributed inside the medium.

2.3. Simplified heuristic model in case $\mu'_{sb} = \mu'_{sbe}$, $\mu_{ab} = \mu_{abe}$ and $n_i = n_e$

In the previous literature we have an example of a heuristic model describing the Raman signal [29,32] obtained under the hypothesis that the optical properties of the background medium at excitation (λ) and emission (λ_e) wavelengths are the same. This model can be true or approximately true in some particular cases of photon migration. Here we want to provide an analytical justification of the heuristic model obtained by Everall et al. [29, 32]. Let's first re-write the general solution $\Phi(\mathbf{r}, t)$ by invoking the very well known scaling relationship for the absorption coefficient [27, 28] (Beer-Lambert's law) as

$$\Phi(\mathbf{r}, \mu_a = \mu_{ab} + \mu_{sR}, \mu'_s, t, \lambda) = \Phi(\mathbf{r}, \mu_a = \mu_{ab}, \mu'_s, t, \lambda) \exp(-\mu_{sR}vt). \quad (8)$$

The evaluation of the fluence rate at λ_e can be obtained under the hypothesis $\mu'_{sb} = \mu'_{sbe}$, $\mu_{ab} = \mu_{abe}$, $v = c/n_i = v_e = c/n_e$ and also assuming the same scattering function of the medium at λ and λ_e and for Tyndall and Raman scattering. This means that the Raman photons at λ_e follow the same identical trajectories, and with the same probability, as they were Tyndall photons at λ and thus subjected to the optical properties of the medium at λ . Thus, the fluence rate at λ_e due to Raman photons, $\Phi_e(\mathbf{r}, \mu_{ae}, \mu'_{se}, t, \lambda_e)$, can be synthetically written as

$$\Phi_e(\mathbf{r}, \mu_{ae} = \mu_{abe}, \mu'_{se} = \mu'_{sbe}, t, \lambda_e) = \Phi_e(\mathbf{r}, \mu_{ab}, \mu'_{sb}, t, \lambda_e). \quad (9)$$

By using the property of Eq. (8) and the described constraints on the optical parameters, the right term of Eq. (9) can be rigorously expressed as

$$\Phi_e(\mathbf{r}, \mu_{ae}, \mu'_{se}, t, \lambda_e) = \Phi(\mathbf{r}, \mu_{ab}, \mu'_{sb}, t, \lambda) - \Phi(\mathbf{r}, \mu_{ab}, \mu'_{sb}, t, \lambda) \exp(-\mu_{sR}vt), \quad (10)$$

i.e. the fluence rate of the whole photons reaching the detector (photons at λ or λ_e are subjected to the same optical parameters) minus the fluence rate of the photons that did *not* undergo a Raman scattering.

Given the typical low values of μ_{sR} (of the order of 10^{-6} mm^{-1}), Eq. (10) can be usually further simplified as

$$\Phi_e(\mathbf{r}, \mu_{ae}, \mu'_{se}, t, \lambda_e) \approx \Phi(\mathbf{r}, \mu_{ab}, \mu'_{sb}, t, \lambda) \mu_{sR}vt. \quad (11)$$

The same relation can be obtained for the TR reflectance. On this ground the heuristic model for the TR reflectance at λ_e , R_{eHeur} , can be written as

$$R_{eHeur}(\rho, \mu_{ae}, \mu'_{se}, t, \lambda_e) = R(\rho, \mu_{ab}, \mu'_{sb}, t, \lambda) \mu_{sR}vt, \quad (12)$$

with ρ source detector distance and R the standard solution of the DE at λ . The solution of the DE for the TR reflectance for the slab obtained with the extrapolated boundary condition and Fick's law can be used for R (see for instance Eq. (4.27) in [28]). Equations (11) and (12) are both the desired Everall et al. model [29,32] obtained under the simplified conditions. Thus, it is possible to directly derive the Green's function of the Raman signal from the Green's function of the background medium and the Raman signals can be obtained by multiplying the diffuse reflectance signal by $\mu_{sR}vt$. The physical interpretation of this simplified model is that the generated Raman photons at the emission wavelength continue their migration in the medium as they were at the excitation wavelength. We can also state that the longer is the photon time-of-flight, the higher is the probability of Raman emission. This heuristic model can only be applied for homogeneous media.

2.4. Solution for the Raman signal in a parallelepiped

2.4.1. Time-resolved fluence rate

The solution for the parallelepiped (Fig. 2) for the fluence rate is obtained using the Green's function calculated with the eigenfunction method. The TR Green function $G(\mathbf{r}, \mathbf{r}', t, t')$ for the fluence rate, making use of the extrapolated boundary conditions (EBC) at the boundaries of the parallelepiped, can be written as [28, 33]

$$G(\mathbf{r}, \mathbf{r}', t) = 2^3 \frac{v}{L'_x L'_y L'_z} \sum_{l,m,n=1}^{\infty} \cos(K_l x) \cos(K_l x') \cos(K_m y) \cos(K_m y') \sin[K_n(z + 2AD)] \sin[K_n(z' + 2AD)] \exp[-(K_l^2 + K_m^2 + K_n^2)Dv(t - t') - \mu_a v(t - t')], \quad (13)$$

with

$$L'_x = L_x + 4AD, \quad L'_y = L_y + 4AD, \quad L'_z = L_z + 4AD, \quad (14)$$

and

$$K_l = \frac{(2l-1)\pi}{L'_x}, \quad K_m = \frac{(2m-1)\pi}{L'_y}, \quad K_n = \frac{n\pi}{L'_z}; \quad l, m, n = 1, 2, 3, 4, 5, \dots \quad (15)$$

The coefficients of Eqs. (14) and (15) will be used in all the next series expansions implemented for the parallelepiped. The coefficient A , that accounts for the effects of Fresnel reflections at the parallelepiped boundaries, is a function of the refractive index of the internal (n_i) and external (n_o) medium ($A = 1$ when $n_i = n_o$ see [28]). The notation A_e will be used when the

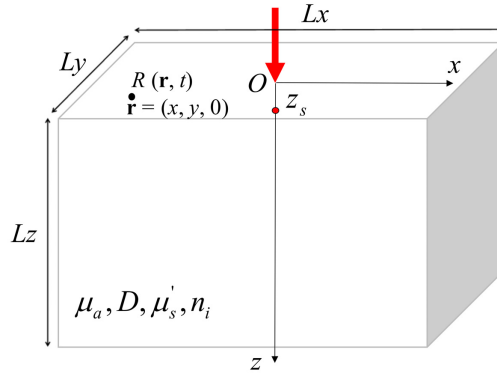


Fig. 2. Schematic of the parallelepiped.

coefficient A pertains to n_{ie} . Making use of Eq. (13) and of the ortho-normality property of the eigenfunctions, the solution of Eq. (7) for the TR fluence rate, assuming an isotropic delta source of unitary strength placed at $(0, 0, z_s = 1/\mu'_s)$ used to model an external pencil beam of unitary strength impinging onto the parallelepiped at $(0, 0, 0)$, i.e. $q(\mathbf{r}, t) = \delta(x)\delta(y)\delta(z - z_s)\delta(t)$, becomes

$$\Phi_{eRaman}(\mathbf{r}, t) = 2^3 \frac{\mu_s R v v_e}{L'_x L'_y L'_z} \sum_{l,m,n=1}^{\infty} \cos(K_l x) \cos(K_m y) \sin[K_n(z + 2A_e D_e)] \times \sin[K_n(z_s + 2AD)] [(D_e v_e - Dv)(K_l^2 + K_m^2 + K_n^2) + (\mu_{ae} v_e - \mu_a v)]^{-1} \times \left\{ \exp[-(K_l^2 + K_m^2 + K_n^2)Dv t - \mu_a v t] - \exp[-(K_l^2 + K_m^2 + K_n^2)D_e v_e t - \mu_{ae} v_e t] \right\}. \quad (16)$$

For obtaining this equation we have assumed, as it is usual, that the extrapolated lengths depend only slightly on λ , and thus, $L'_{xe} \cong L'_x$, $L'_{ye} \cong L'_y$, and $L'_{ze} \cong L'_z$ since $L_x \gg 4AD$, $L_y \gg 4AD$, $L_z \gg 4AD$. The same approximation is used throughout this paper. Once more we remind that $\mu_a = \mu_{ab} + \mu_{sR}$ and $\mu_{ae} = \mu_{abe}$. A similar solution to Eq. (16) for the fluence rate is obtained in appendix A also for the finite cylinder.

The TR Raman reflectance from the external surface of the parallelepiped at any point \mathbf{r} of the boundary can be obtained using Fick's law or a hybrid approach denoted EBPC [28]. For both the approaches the Raman fluence rate, Φ_{eRaman} , (Eq. (16)) is first calculated using the EBC, then Fick's law or the partial current boundary condition (PCBC) is applied to Eq. (16) for calculating the emerging reflectance from the medium [28].

2.4.2. Time-resolved reflectance obtained with the EBPC

According to the EBPC the TR Raman reflectance is [28]

$$R_{eRamanEBPC}(x, y, t) = \frac{\Phi_{eRaman}(x, y, z=0, t)}{2A_e}. \quad (17)$$

By substituting Eq. (16) in Eq. (17) we obtain the TR Raman reflectance as

$$\begin{aligned} R_{eRamanEBPC}(x, y, t) = & 2^2 \frac{\mu_{sR} \nu \nu_e}{A_e L'_x L'_y L'_z} \sum_{l,m,n=1}^{\infty} \cos(K_l x) \cos(K_m y) \sin[K_n (2A_e D_e)] \\ & \times \sin[K_n (z_s + 2AD)] [(D_e \nu_e - D\nu)(K_l^2 + K_m^2 + K_n^2) + (\mu_{ae} \nu_e - \mu_a \nu)]^{-1} \\ & \times \left\{ \exp[-(K_l^2 + K_m^2 + K_n^2) D \nu t - \mu_a \nu t] - \exp[-(K_l^2 + K_m^2 + K_n^2) D_e \nu_e t - \mu_{ae} \nu_e t] \right\}. \end{aligned} \quad (18)$$

2.4.3. Time-resolved reflectance with Fick's law

The TR Raman reflectance from the medium can be also calculated by using the classical Fick's law as [28]

$$R_{eRamanFick}(x, y, t) = D_e \frac{\partial \Phi_{eRaman}(x, y, z=0, t)}{\partial z}. \quad (19)$$

By inserting Eq. (16) in Eq. (19) the TR Raman reflectance becomes

$$\begin{aligned} R_{eRamanFick}(x, y, t) = & 2^3 \frac{D_e \mu_{sR} \nu \nu_e}{L'_x L'_y L'_z} \sum_{l,m,n=1}^{\infty} \cos(K_l x) \cos(K_m y) K_n \cos[K_n (2A_e D_e)] \\ & \times \sin[K_n (z_s + 2AD)] [(D_e \nu_e - D\nu)(K_l^2 + K_m^2 + K_n^2) + (\mu_{ae} \nu_e - \mu_a \nu)]^{-1} \\ & \times \left\{ \exp[-(K_l^2 + K_m^2 + K_n^2) D \nu t - \mu_a \nu t] - \exp[-(K_l^2 + K_m^2 + K_n^2) D_e \nu_e t - \mu_{ae} \nu_e t] \right\}. \end{aligned} \quad (20)$$

The two expressions of $R_{eRamanEBPC}$ and $R_{eRamanFick}$ show only slight differences related to the way the flux is calculated [28]. In the Results section comparisons with the results of MC simulations show that within the limits of the DA the two formulas are practically equivalent.

2.5. Solution for the Raman signal with a background fluorescence

2.5.1. Time-resolved fluence rate

It may happen that a fluorescence signal survives at the detector's site when Raman spectroscopic measurements are carried out or, alternatively, fluorescence and Raman signals can be indeed used together for imaging and/or spectroscopic purposes [34]. For this reason, we generalize the previous solution in the event that, together with Raman scatterers, fluorescent molecules are also uniformly distributed inside the medium generating a background fluorescence at λ_e (observed wavelength). The fluorescence signal, as the Raman scattered light, is affected by multiple Tyndall scattering at both λ and λ_e . We assume that a fluorophore is uniformly distributed inside the background medium with absorption coefficient μ_{af} at λ , and $\mu_{afe} = 0$ at λ_e . As in the previous section, we also assume that Raman scatterers are distributed inside the whole volume of the medium with scattering coefficient μ_{sR} at λ , and $\mu_{sRe} = 0$ at λ_e . The global optical parameters: absorption coefficient, reduced scattering coefficient, and the refractive index of the medium are denoted as μ_a , μ'_s , and n at λ , and as μ_{ae} , μ'_{se} , and n_e at λ_e , respectively. Therefore, we implement the DE solution for a medium having the global optical properties, $\mu_a = \mu_{ab} + \mu_{sR} + \mu_{af}$, $\mu'_s = \mu'_{sb}$ at λ and, $\mu_a = \mu_{abe}$ and $\mu'_{se} = \mu'_{sbe}$ at λ_e , respectively. For

this purpose we can still use Eqs. (1) and (2) provided the optical properties are those shown in Table 1 for the case of Raman+Fluorescence.

Again, the DEs at λ and λ_e are coupled by the excitation fluence rate, Φ , which determines the source term $q_e(\mathbf{r}, t)$ of the DE at λ_e . However, the fluorescent component of the source term $q_e(\mathbf{r}, t)$ is more complicated than the Raman component. In fact, not all the fluorescence interactions at λ produce a photon at λ_e . Moreover, fluorescent photons at λ_e , generated at time t , may be derived from fluorescence interactions occurring at a time t' different from t ($t' < t$). For these reasons, it is necessary to define: 1) a quantum efficiency η_e and; 2) a probability density function $p_{Fluo}(t | t')$. The parameter η_e is the quantum efficiency of the fluorophore in the wavelength range $\Delta\lambda_e$ around λ_e , i.e. the ratio of the number of photons emitted in $\Delta\lambda_e$ to the number of absorbed photons. The function $p_{Fluo}(t | t')$ is expressed as

$$p_{Fluo}(t | t') = \frac{1}{\tau} \exp\left(-\frac{t-t'}{\tau}\right) \Theta(t-t'), \quad (21)$$

($\int p_{Fluo}(t | t') dt' = 1$) and describes the probability density that an interaction at t' will generate a photon at t . The function $\Theta(\cdot)$ is the Heaviside function. The parameter τ is the fluorescence lifetime of the fluorophore (i.e. the average time that the fluorophore spends in the excited state prior to returning to the ground state). In practice, the production of fluorescent photons must be suitably “weighted” by η_e and $p_{Fluo}(t | t')$. Therefore, in analogy with Sec. 2.2 the coupling of the DE at λ and λ_e is given by the following source term that combines fluorescent and Raman emitted photons

$$q_e(\mathbf{r}', t) = \int_0^t p_{Fluo}(t | t') \eta_e \mu_{af} G(\mathbf{r}_s, \mathbf{r}', \mu_a, \mu'_s, n, t') dt' + \mu_{sR} G(\mathbf{r}_s, \mathbf{r}', \mu_a, \mu'_s, n, t), \quad (22)$$

where G is the Green's function for the fluence rate at λ .

By substituting Eq. (22) in the DE at λ_e , and making use of the Green's function theorem, the fluence rate at the emission wavelength, $\Phi_e(\mathbf{r}, t)$, due to the fluorescent photons generated into the interval $d\lambda_e$, is

$$\begin{aligned} \Phi_e(\mathbf{r}, t) &= \int_0^t \int_{V'} q_e(\mathbf{r}', t') G_e(\mathbf{r}', \mathbf{r}, \mu_{ae}, \mu'_{se}, n_e, t-t') d\mathbf{r}' dt' = \\ &= \Phi_{eFluo}(\mathbf{r}, t) + \Phi_{eRaman}(\mathbf{r}, t), \end{aligned} \quad (23)$$

with G_e as the Green's function of the medium for the fluence rate at λ_e . The solution of Eq. (23) is given by two terms, one, $\Phi_{eFluo}(\mathbf{r}, t)$, given by fluorescent photons and the other, $\Phi_{eRaman}(\mathbf{r}, t)$, given by Raman photons. The term Φ_{eRaman} is the one calculated in the previous section with Eq. (16). For the term Φ_{eFluo} we need to perform the integral of Eq. (23) for the fluorescence source term. For the parallelepiped the TR solution is obtained by making use of the TR Green's function given by Eq. (13) and applying the orthogonality property of the eigenfunctions. The solution given by Eq. (23) for the TR fluence rate, Φ_{eFluo} , assuming an isotropic delta source of unitary strength placed at $(0, 0, z_s = 1/\mu'_s)$, i.e.

Table 1. Summary of the notations used for the optical properties of the medium at λ and λ_e in the case of a pure Raman model (column Raman) or a hybrid Raman and fluorescence model (column Raman+Fluorescence). The subscript b denotes the background, the subscript R denotes the Raman scattering and the subscript f denotes the fluorescence. In this work, we have assumed $\mu_{sR} = 0$ and $\mu_{afe} = 0$. The optical parameters appearing in column Raman have to be used with Eqs. (18), (20) and (39), while optical parameters appearing in column Raman+Fluorescence have to be used with Eqs. (24), (28) and (32).

Raman				Raman+Fluorescence			
λ		λ_e		λ		λ_e	
μ_a	μ'_s	μ_{ae}	μ'_{se}	μ_a	μ'_s	μ_{ae}	μ'_{se}
$\mu_{ab} + \mu_{sR}$	μ'_{sb}	μ_{abe}	μ'_{sbe}	$\mu_{ab} + \mu_{sR} + \mu_{af}$	μ'_{sb}	μ_{abe}	μ'_{sbe}

$q(\mathbf{r}, t) = \delta(x)\delta(y)\delta(z - z_s)\delta(t)$, is

$$\begin{aligned}
\Phi_{eFluo}(\mathbf{r}, t) &= 2^3 \frac{\mu_{af}\eta_e v v_e}{\tau L_x L_y L_z} \sum_{l,m,n=1}^{\infty} \cos(K_l x) \cos(K_m y) \sin[K_n(z + 2A_e D_e)] \\
&\times \sin[K_n(z_s + 2AD)] [(D_e v_e - Dv)(K_l^2 + K_m^2 + K_n^2) + (\mu_{ae} v_e - \mu_a v)]^{-1} \\
&\times \left\{ \exp[-(K_l^2 + K_m^2 + K_n^2) D v t - \mu_a v t] - \exp[-(K_l^2 + K_m^2 + K_n^2) D_e v_e t - \mu_{ae} v_e t] \right\} \\
&\times \left[-(K_l^2 + K_m^2 + K_n^2) D v - \mu_a v + 1/\tau \right]^{-1} \\
&- 2^3 \frac{\mu_{af}\eta_e v v_e}{\tau L_x L_y L_z} \sum_{l,m,n=1}^{\infty} \cos(K_l x) \cos(K_m y) \sin[K_n(z + 2A_e D_e)] \\
&\times \sin[K_n(z_s + 2AD)] [(K_l^2 + K_m^2 + K_n^2) D_e v_e + \mu_{ae} v_e - 1/\tau]^{-1} \\
&\times \left\{ \exp[-t/\tau] - \exp[-(K_l^2 + K_m^2 + K_n^2) D_e v_e t - \mu_{ae} v_e t] \right\} \\
&\times \left[-(K_l^2 + K_m^2 + K_n^2) D v - \mu_a v + 1/\tau \right]^{-1}.
\end{aligned} \tag{24}$$

We note that, for the evaluation of the Eq. (23) we have previously calculated the first term of $q_e(\mathbf{r}', t')$, $q_{eFluo}(\mathbf{r}', t')$, (Eq. (22)) as

$$\begin{aligned}
q_{eFluo}(\mathbf{r}', t') &= \frac{\mu_{af}}{\tau} \eta_e \int_0^{t'} \exp\left[-\frac{(t'-t'')}{\tau}\right] G(\mathbf{r}_s, \mathbf{r}', \mu_a, \mu'_s, n, t'') dt'' = \\
&= 2^3 \frac{\eta_e \mu_{af} v}{\tau L_x L_y L_z} \sum_{l,m,n=1}^{\infty} \cos(K_l x_s) \cos(K_l x') \cos(K_m y_s) \cos(K_m y') \sin[K_n(z_s + 2AD)] \\
&\times \sin[K_n(z' + 2AD)] \left[-(K_l^2 + K_m^2 + K_n^2) D v - \mu_a v + 1/\tau \right]^{-1} \\
&\times \left\{ \exp[-(K_l^2 + K_m^2 + K_n^2) D v t' - \mu_a v t'] - \exp[-t'/\tau] \right\},
\end{aligned} \tag{25}$$

with G given by Eq. (13).

2.5.2. Time-resolved reflectance with EBPC

The TR reflectance can be calculated using the EBPC, similarly to Eq. (17), as

$$R_{eEBPC}(x, y, \lambda_e, t) = \frac{\Phi_{eFluo}(x, y, z=0, \lambda_e, t)}{2A_e} + \frac{\Phi_{eRaman}(x, y, z=0, \lambda_e, t)}{2A_e}, \tag{26}$$

where Φ_{eFluo} is given by Eq. (24) and Φ_{eRaman} by Eq. (16).

2.5.3. Time-resolved reflectance with Fick's law

The time resolved reflectance can be also calculated by using Fick's law as

$$\begin{aligned}
R_{eFick}(x, y, t) &= D_e \frac{\partial \Phi_{eFluo}(x, y, z=0, \lambda_e, t)}{\partial z} + D_e \frac{\partial \Phi_{eRaman}(x, y, z=0, \lambda_e, t)}{\partial z} = \\
&= R_{eFluoFick}(x, y, t) + R_{eRamanFick}(x, y, t),
\end{aligned} \tag{27}$$

with $R_{eRamanFick}$ given by Eq. (20) and $R_{eFluoFick}$ given by

$$\begin{aligned}
R_{eFluoFick}(x, y, t) &= 2^3 \frac{D_e \mu_{af} \eta_e v v_e}{\tau L_x' L_y' L_z'} \sum_{l,m,n=1}^{\infty} \cos(K_l x) \cos(K_m y) K_n \cos[K_n(2A_e D_e)] \\
&\times \sin[K_n(z_s + 2AD)] [(D_e v_e - Dv)(K_l^2 + K_m^2 + K_n^2) + (\mu_{ae} v_e - \mu_a v)]^{-1} \\
&\times \left\{ \exp[-(K_l^2 + K_m^2 + K_n^2) D v t - \mu_a v t] - \exp[-(K_l^2 + K_m^2 + K_n^2) D_e v_e t - \mu_{ae} v_e t] \right\} \\
&\times \left[-(K_l^2 + K_m^2 + K_n^2) D v - \mu_a v + 1/\tau \right]^{-1} \\
&- 2^3 \frac{D_e \mu_{af} \eta_e v v_e}{\tau L_x' L_y' L_z'} \sum_{l,m,n=1}^{\infty} \cos(K_l x) \cos(K_m y) K_n \cos[K_n(2A_e D_e)] \\
&\times \sin[K_n(z_s + 2AD)] [(K_l^2 + K_m^2 + K_n^2) D_e v_e + \mu_{ae} v_e - 1/\tau]^{-1} \\
&\times \left\{ \exp[-t/\tau] - \exp[-(K_l^2 + K_m^2 + K_n^2) D_e v_e t - \mu_{ae} v_e t] \right\} \\
&\times \left[-(K_l^2 + K_m^2 + K_n^2) D v - \mu_a v + 1/\tau \right]^{-1}.
\end{aligned} \tag{28}$$

2.5.4. Improved numerical calculation

The formula obtained above for Φ_{eFluo} suffers from slow computational convergence so that usually many terms of the series are needed for a correct evaluation of the fluence rate. A simple way to speed-up the calculation is achieved by dividing the calculation of Φ_{eFluo} into two steps. At first is calculated the fluence rate, Φ_{e0Fluo} , describing fluorescence photons promptly re-emitted (i.e. Eq. (24) for $\tau \rightarrow 0$). The series of Φ_{e0Fluo} converges much faster than Φ_{eFluo} . The fluence rate Φ_{e0Fluo} is simply given by

$$\begin{aligned}
\Phi_{e0Fluo}(\mathbf{r}, t) &= \mu_{af} \eta_e \int_0^t \int_{V'} G(\mathbf{r}_s, \mathbf{r}', \mu_a, \mu_s t', n, t') G_e(\mathbf{r}', \mathbf{r}, \mu_{ae}, \mu_{se} t', n_e, t - t') d\mathbf{r}' dt' = \\
&= 2^3 \frac{\mu_{af} \eta_e v v_e}{L_x' L_y' L_z'} \sum_{l,m,n=1}^{\infty} \cos(K_l x) \cos(K_m y) \sin[K_n(z + 2A_e D_e)] \sin[K_n(z_s + 2AD)] \\
&\times [(D_e v_e - Dv)(K_l^2 + K_m^2 + K_n^2) + (\mu_{ae} v_e - \mu_a v)]^{-1} \\
&\times \left\{ \exp[-(K_l^2 + K_m^2 + K_n^2) D v t - \mu_a v t] - \exp[-(K_l^2 + K_m^2 + K_n^2) D_e v_e t - \mu_{ae} v_e t] \right\}.
\end{aligned} \tag{29}$$

Then, the calculation of the whole term Φ_{eFluo} is obtained by taking into account that fluorescent photons are not promptly re-emitted. Therefore, Φ_{eFluo} may be expressed as the convolution of Φ_{e0Fluo} with the exponential decay of the fluorophore, i.e.

$$\Phi_{eFluo}(\mathbf{r}, t) = [\Phi_{e0Fluo}(\mathbf{r}, t)] * \left[\frac{1}{\tau} \exp(-t/\tau) \right]. \tag{30}$$

This calculation in two steps is computationally much faster (even ten times) than the direct calculation of Eq. (24). Moreover, the implementation of Eq. (30) can be easily modified in order to account for more complicated multi-exponential decays that sometimes are required to describe the re-mission of some specific fluorophores.

Similarly, the improved numerical calculation can be obtained for the fluorescence reflectance term as

$$R_{eFluo}(\mathbf{r}, t) = [R_{e0Fluo}(\mathbf{r}, t)] * \left[\frac{1}{\tau} \exp(-t/\tau) \right]. \tag{31}$$

When the reflectance is calculated with the EBPC, R_{e0Fluo} is obtained by dividing Φ_{e0Fluo} by a factor $2A_e$ according to Eq. (26). When the reflectance is calculated with Fick's law, R_{e0Fluo} is obtained as

$$\begin{aligned}
R_{e0FluoFick}(x, y, t) &= 2^3 \frac{D_e \mu_{af} \eta_e v v_e}{L_x' L_y' L_z'} \sum_{l,m,n=1}^{\infty} \cos(K_l x) \cos(K_m y) K_n \cos[K_n(2A_e D_e)] \\
&\times \sin[K_n(z_s + 2AD)] [(D_e v_e - Dv)(K_l^2 + K_m^2 + K_n^2) + (\mu_{ae} v_e - \mu_a v)]^{-1} \\
&\times \left\{ \exp[-(K_l^2 + K_m^2 + K_n^2) D v t - \mu_a v t] - \exp[-(K_l^2 + K_m^2 + K_n^2) D_e v_e t - \mu_{ae} v_e t] \right\}.
\end{aligned} \tag{32}$$

2.6. Monte Carlo simulations

It is useful, for the comprehension and validation of the analytical approach proposed in the previous sections, to address and simulate Raman scattering, also in the presence of background fluorescence, using a Monte Carlo method without introducing approximations in the modelling of photon transport [28, 29]. Following the notations of Sec. 2.5 we define an interaction coefficient, $\mu_{e\lambda}$, at the excitation wavelength as:

$$\mu_{e\lambda} = \mu_{ab} + \mu_{sb} + \mu_{sR} + \mu_{af}, \quad (33)$$

where the right hand side is the sum of the four coefficients of: absorption in the background, Tyndall scattering in the background, Raman scattering and fluorescence excitation. A random number w_1 uniformly distributed in the interval $[0, 1]$ is generated. This number is related to the photon path, ℓ , by the following relation [35]:

$$w_1 = \int_0^\ell \mu_{e\lambda} \exp(-\mu_{e\lambda} \ell) d\ell. \quad (34)$$

Once Eq. (34) is inverted to obtain ℓ we have to decide which interaction the photon will undergo. To sample the probability of the four different events we extract a second random number w_2 uniformly distributed in $[0, 1]$, so that:

- if $w_2 < \frac{\mu_{ab}}{\mu_{e\lambda}}$ the photon is absorbed, otherwise
- if $w_2 < \frac{\mu_{ab} + \mu_{sb}}{\mu_{e\lambda}}$ the photon is Tyndall scattered, otherwise
- if $w_2 < \frac{\mu_{ab} + \mu_{sb} + \mu_{sR}}{\mu_{e\lambda}}$ the photon is Raman scattered, otherwise
- if $w_2 \leq 1$ the photon possibly excites fluorescence.

When the photon is absorbed its propagation is stopped; when it is Tyndall scattered, the photon is tagged as “ λ ” (the wavelength remains λ), the scattering angle is sampled [35] and it moves of a step-length equal to ℓ ; when it is Raman scattered the photon is tagged as “ λ_e ” (from now on the photon can only have Tyndall scattering events at λ_e), an isotropic scattering angle is sampled and it moves of a step-length equal to ℓ ; when it possibly excites fluorescence a further random number $w_3 \in [0, 1]$ is extracted and, if $w_3 < \eta$, the photon is tagged again as “ λ_e ” and it propagates with a step-length ℓ (from now on the photon can only have Tyndall scattering events at λ_e), otherwise the photon is *killed*. Furthermore, if the photon excites fluorescence, a temporal delay is extracted using a new random number $w_4 \in [0, 1]$ sampling the exponential decay time (Eq. (21)):

$$w_4 = \int_0^t p_{Fluo}(t' | 0) dt'. \quad (35)$$

The photons tagged as “ λ_e ” represent photons at the emission wavelength then, assuming that no further Raman scattering events are undergone by photons, and they propagate as described above using a new interaction coefficient $\mu_{e\lambda_e}$ given by:

$$\mu_{e\lambda_e} = \mu_{abe} + \mu_{sbe}. \quad (36)$$

At the beginning of the simulation it is possible to select the kind of interaction (Raman, fluorescence, Raman+fluorescence or Tyndall) and the number of photons that, after surviving at the detector site, need to be saved and stored by the simulation. In particular, the path-length of the tagged photons arriving at the detector site is saved and then a time-of-flight histogram is created so the TR reflectance can be re-constructed from the detected photons packets.

3. Results

3.1. Validation of the DE solutions by comparisons with MC simulations

The analytical solutions derived in Sec. 2.5 have been compared with the results of MC simulations based on the sampling rules described in Sec. 2.6. The code was accelerated by means of a Graphical Processing Unit (GPU) and has been written adapting the CUDA-based code published by Alerstam et al. [36] for a laterally infinite slab. A large number of comparisons between analytical models and MC simulations have been performed to validate the formulae of Sec. 2.5 and those shown in this section are only a representative sample of the whole work done.

Simulated reflectance data have been generated with the optical parameters appearing in the caption of Fig. 3. All the simulations have been run until 10^7 photons reached the detector. The analytical models have been computed using the formulae presented in Sec. 2.5 applied to a $100 \times 100 \times 100$ mm³ diffusive cube. The boundary effects due to photons escaping the lateral faces of the cube are negligible for the values of the optical properties used in this section.

Although the probability of generating a Raman photon is low, with typical values of about 10^{-6} , for the validation of the analytical models we have assumed unrealistic values of this probability with values around 10^{-3} . This was obtained by selecting $\mu_{sR} = 10^{-3}$ mm⁻¹. This choice, needed for reducing the computation time of the MC simulations, does not affect the validation of the analytical models. In fact, the accuracy of the analytical models, provided that $\mu_{sR} \ll \mu_{sb}$, is not affected by the value of μ_{sR} considered.

In Fig. 3 four examples of comparison of the analytical models (EBPC and Fick solutions) with the results MC simulations for the TR Raman-Fluorescence reflectance are shown. Starting from the first simulation (Fig. 3(a)-3(b)), the others have been obtained by varying one parameter at a time: μ_{af} (Fig. 3(c)-3(d)), another with a different ρ (Fig. 3(e)-3(f)) and the remaining one with a different μ_{ab} (Fig. 3(g)-3(h)). We note that the optical properties used for the background medium are typical of several biological tissues. It is also worth to observe the excellent agreement between analytical models and MC results.

The slight differences between Fick and EBPC model are typical of the DA and, as for many other solutions based on the DE, they are mainly affecting the early times of the TR reflectance. The Fick and EBPC solutions slightly differ on the peak of the signal. In particular, EBPC overestimates the photon fluence rate. At late times and in absence of fluorescence the two formulae converge (Fig. 3(b)).

In the presence of a background fluorescence (Fig. 3(c)), the agreement between Fick's law formula and MC is still very good and slightly worse for the EBPC formula because the fluence rate overestimation on the peak is spread out at late times. This is due to the convolution operation appearing in Eq. (31). This effect is clearly noticeable in Fig. 3(d) by plotting the ratio of analytical solutions and MC. But we can note that this overestimation of the signal has a mild effect on the shape of the TR reflectance generated with the EBPC.

3.2. Dependence of the Raman signal on the optical properties

The factor μ_{sR} appearing in Eqs. (18) and (20) clearly shows that the TR Raman reflectance is proportional to the Raman scattering coefficient. In practice, μ_{sR} is just a simple amplitude factor and does not influence the shape of the temporal profile. However, Eqs. (18) and (20) also show that the TR Raman reflectance depends on absorption and reduced scattering coefficients in a more complex manner. In Fig. 4 we have reported this feature by displaying the TR Raman reflectance with: 1) varying μ_{abe} , fixed μ_{ab} and fixed $\mu'_{sb} = \mu'_{sbe}$ and; 2) varying $\mu'_{sb} = \mu'_{sbe}$ and fixed $\mu_{ab} = \mu_{abe}$. The values of the optical parameters appear in the caption of Fig. 4. The ranges of the background optical properties in Fig 4 include those of biological media in the wavelength range of [700, 900] nm. The general trend is similar to what observed in

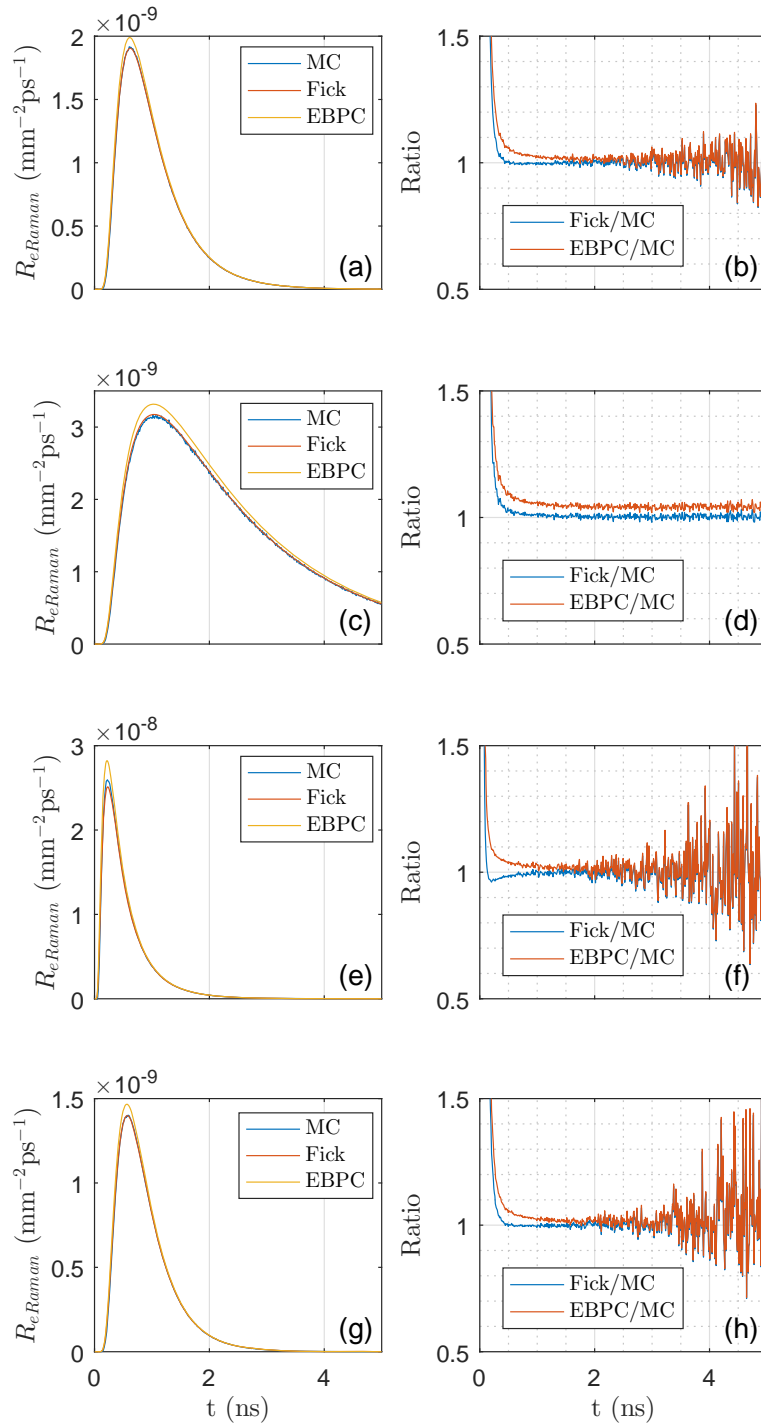


Fig. 3. Comparison for the TR Raman reflectance between analytical formulae and MC in absence (a, e, g) and in presence (c) of background fluorescence. For all the figure panels $\mu'_{sb} = \mu'_{sbe} = 1$, $\mu_{abe} = 7 \cdot 10^{-3} \text{ mm}^{-1}$, $\mu_{sR} = 10^{-3} \text{ mm}^{-1}$, $n_i = n_{ie} = 1.4$, $n_o = n_{oe} = 1$, $g = 0$. Specifically: (a) $\mu_{ab} = 5 \cdot 10^{-3} \text{ mm}^{-1}$, $\mu_{af} = 0$, $\rho = 20 \text{ mm}$; (c) $\mu_{ab} = 5 \cdot 10^{-3} \text{ mm}^{-1}$, $\mu_{af} = 7 \cdot 10^{-3} \text{ mm}^{-1}$, $\eta_e = 1$ and $\tau = 2 \text{ ns}$, $\rho = 20 \text{ mm}$; (e) $\mu_{ab} = 5 \cdot 10^{-3} \text{ mm}^{-1}$, $\mu_{af} = 0$, $\rho = 10 \text{ mm}$; (g) $\mu_{ab} = 10^{-2} \text{ mm}^{-1}$, $\mu_{af} = 0$, $\rho = 20 \text{ mm}$.

standard TR diffuse optical spectroscopy, with a decrease of signal more prominent at late times for increased absorption (Fig. 4(a)), and at early times for increased scattering (Fig. 4(b)). In conclusion, Fig. 4 show that the TR Raman signal carries information not only of the Raman phenomenon, but also on the background properties of the medium.

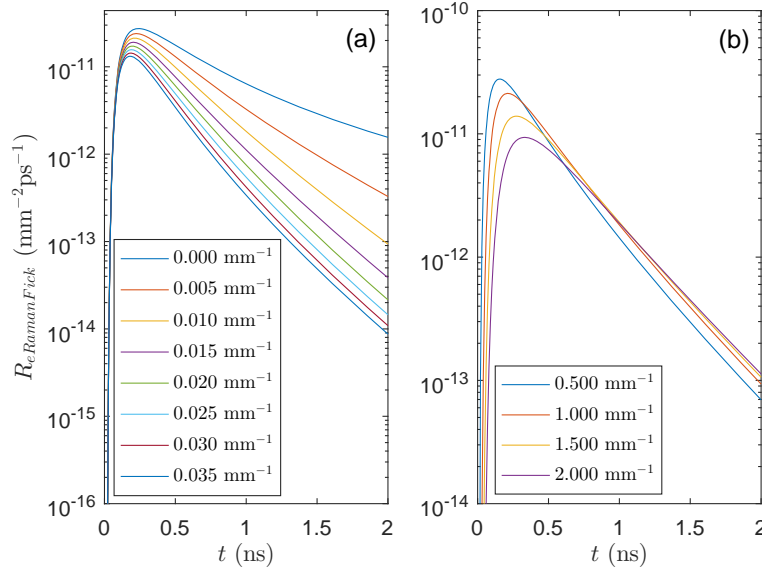


Fig. 4. Dependence of the temporal profile of Raman photons for different values of μ_{abe} and μ'_{sb} . The common parameters were $\rho = 10$ mm, $n_i = n_{ie} = 1.4$, $n_o = n_{oe} = 1$ and $\mu_{sR} = 10^{-6}$ mm $^{-1}$, $\mu_{ab} = 0.01$ mm $^{-1}$. Specifically: **(a)** $\mu_{abe} \in [0, 0.035]$ mm $^{-1}$ and $\mu'_{sb} = \mu'_{sbe} = 1$ mm $^{-1}$ and; **(b)** $\mu'_{sb} = \mu'_{sbe} \in [0.5, 2]$ mm $^{-1}$ and $\mu_{abe} = 0.01$ mm $^{-1}$.

3.3. Validity range of the heuristic model

As already demonstrated in Sec. 2.3 the heuristic model proposed in [29, 32] by Everall et al. is actually a simplified model derived under the constraints of $\mu'_{sb} = \mu'_{sbe}$, $\mu_{ab} = \mu_{abe}$ and $n_i = n_e$. Here we want to study the range of validity of the heuristic model by means of the forward solvers discussed and validated in the present work. More specifically, we study the effect given by the release of the above constraints.

Figure 5 shows an example of the TR Raman signal (Eq. (20)) and of the heuristic model (Eq. (12)) for a case with $\mu'_{sb} \neq \mu'_{sbe}$ (see figure caption for the values of the optical parameters). The figure shows that the heuristic model fails in describing the correct behavior.

In Fig. 6 the differences observed in Fig. 5 are studied in a larger number of cases in order to provide a more complete view of the validity range of Eq. (20). To this aim we define a relative error factor, $\epsilon(t)$, comparing the heuristic model (Eq. (12)) with the rigorous solution (Eq. (20)):

$$\epsilon(t) = 1 - \frac{R_{eHeur}(\rho, t)}{R_{eRamanFick}(\rho, t)}. \quad (37)$$

The error $\epsilon(t)$ is depicted in Fig. 6 in per cent for different values of μ_{abe} (Fig. 6(a)) or of μ'_{sbe} (Fig. 6(b)) while keeping both μ_{ab} and μ'_{sb} fixed. The relative error is null when μ_{ab} and μ_{abe} have the same values, while it rapidly deviates with huge errors whenever μ_{abe} is significantly altered from μ_{ab} . For example, in biological tissues, for Raman shifts in the range of [30, 50] nm a change of μ_{abe} in the range of [0.005, 0.01] mm $^{-1}$ can be expected for an excitation wavelength in the range of [700, 800] nm. In case we have a change of scattering between λ and

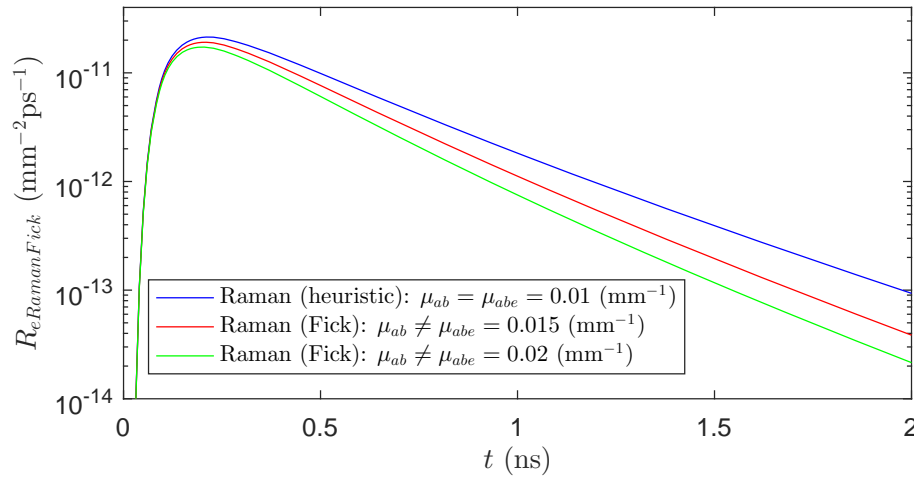


Fig. 5. Comparison of the temporal profile of the DE Raman signal (Eq. (20)), and of the heuristic model (Eq. (12)). The common parameters were: $\rho = 10$ mm, $n_i = n_{ie} = 1.4$, $n_o = n_{oe} = 1$, $\mu_{sR} = 10^{-6}$ mm $^{-1}$, $\mu'_{sb} = \mu'_{sbe} = 1$ mm $^{-1}$, and $\mu_{ab} = 0.01$ mm $^{-1}$.

λ_e , the heuristic model is substantially valid at late times, but yields quite inaccurate predictions at early times. Thus, Eq. (12) can be used as a first-order approximation to understand the physics of diffuse Raman photons, but a more rigorous approach is needed when the absorption properties of the medium are not constant over the spectral range of interest.

4. Conclusions

We have presented, within the framework of the DE, a set of analytical forward solvers for the calculation of the Raman TR reflectance from a homogeneous parallelepiped and a homogeneous cylinder, provided the Raman scatterers are uniformly distributed in the whole medium. The obtained formulas have been validated by means of comparisons with the results of “gold standard” MC simulations. In the proposed analytical solutions we have also included the option to account for the influence of a background fluorescence, on the Raman signal, generated by a fluorophore uniformly distributed inside the medium. Further, we have provided an exact theoretical justification of a well known heuristic model; widely used for the study of the Raman signal when the optical properties of the medium show weak variations between the excitation and the emission wavelength. Thanks to the present results, it has been possible to carefully study the range of validity of the heuristic model.

The comparisons between analytical models and MC simulations of Sec. 3 have shown that in the diffusive regime the analytical solutions (Eqs. (18) and (20)) of the DE for the TR Raman reflectance show indistinguishable results compared to the MC simulations. The differences between Fick and EBPC model are compatible with the diffusion approximation and both can be used to describe the Raman signal with an error of few per cent. Similar conclusions can be extended to the effect of a background fluorescence that can be accurately calculated by the DE analytical solutions (Eqs. (28) and (26)) with an error of few per cent. The computation time of such models is of the order of seconds, while the computation time of the corresponding MC simulation, although the simulation was accelerated by means of a GPU, was of the order of hours. Moreover, when the MC simulations are carried for realistic values of the Raman scattering coefficient (of the order of 10^{-6} mm $^{-1}$) the computation time can be even thousand time larger, becoming prohibitively high. The comparisons with the results of MC simulations have shown that the heuristic model (Eqs. (11) and (12)) has significant deficiencies when the absorp-

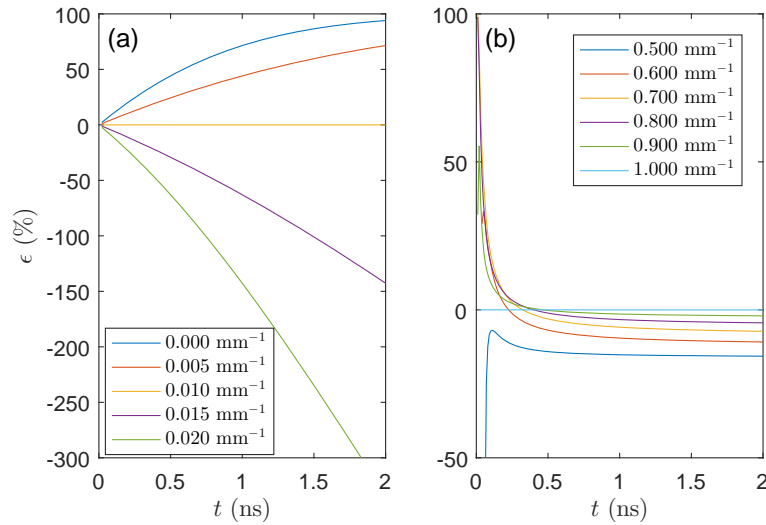


Fig. 6. Relative per cent error of the heuristic model (Eq. (12)) as compared to the DE solver (Eq. (20)). The common parameters were $\rho = 10$ mm, $n_i = n_{ie} = 1.4$, $n_o = n_{oe} = 1$, $\mu_{sR} = 10^{-6}$ mm^{-1} , $\mu_{ab} = 0.01$ mm^{-1} and $\mu'_{sb} = 1$ mm^{-1} . Specifically: (a) $\mu_{abe} \in [0, 0.02]$ mm^{-1} and $\mu'_{sbe} = 1$ mm^{-1} and; (b) $\mu'_{sbe} \in [0.5, 1]$ mm^{-1} and $\mu_{abe} = 0.01$ mm^{-1} .

tion coefficient varies between the excitation and the emission wavelength, while the changes of scattering affect the accuracy of the model only at early times. In practice, the proposed forward solvers based on the DE are suitable tools for studying the TR Raman signal in diffusion conditions, while the heuristic model can only provide an approximate solution that is consistent with the DE when the optical properties at excitation and emission wavelengths are coincident.

In conclusion, the proposed forward solvers can be a useful tool for exploring the information content encoded in the TR Raman measurements. The use of these solvers will allow one to depict, in a wide perspective, possible new applications derived from time-domain Raman measurements.

A. Appendix: DE solution for a finite cylinder

We provide here the solution of the DE for the Raman signal for the finite cylinder. This solution for the fluence rate is obtained with the same procedure used for the parallelepiped in Sec. 2.4, provided the radial eigenfunctions are taken equal to the Bessel functions of the first kind of order zero J_0 . Given a finite cylinder (see Fig. 7) of thickness s , radius a , with the z axis along the main axis of the cylinder, and with ρ the distance between the position \mathbf{r} and the z axis, the Green's function with the EBC of the DE for the finite cylinder of Fig. 7 can be written as [28,33]

$$G(\mathbf{r}, \mathbf{r}', t) = 2 \frac{v}{\pi a'^2 s'} \sum_{l=1}^{\infty} \sum_{n=1}^{\infty} \frac{J_0(\rho \lambda_l) J_0(\rho' \lambda_l)}{J_1^2(a' \lambda_l)} \sin[K_n(z + 2AD)] \sin[K_n(z' + 2AD)] \exp[-\lambda_l^2 D v(t - t')] \exp[-K_n^2 D v(t - t')] \exp[-\mu_a v(t - t')], \quad (38)$$

with $a' = a + 2AD$, $s' = s + 4AD$, $K_n = n\pi/s'$, λ_l roots of $J_0(\lambda_l a') = 0$, J_0 Bessel function of the first kind of order zero and J_1 Bessel function of the first kind of order one. Making use of Eq. (38) and of the ortho-normality property of the eigenfunctions, the solution of Eq. (7) for the TR fluence rate, assuming an isotropic delta source of unitary strength placed at (0,

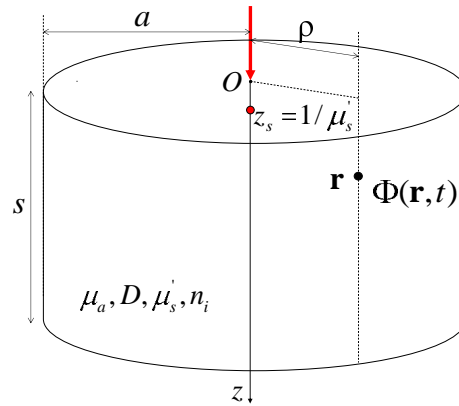


Fig. 7. Schematic of a diffusive cylinder.

0, $z_s = 1/\mu_s'$ used to model an external pencil beam of unitary strength impinging onto the cylinder at (0, 0, 0), i.e. $q(\mathbf{r}, t) = \delta(x)\delta(y)\delta(z - z_s)\delta(t)$, becomes

$$\begin{aligned} \Phi_{eRamanCyl}(\mathbf{r}, t) &= 2 \frac{\mu_s R v v_e}{\pi a'^2 s'} \sum_{l=1}^{\infty} \sum_{n=1}^{\infty} \frac{J_0(\rho \lambda_l)}{J_1^2(a' \lambda_l)} \sin[K_n(z + 2A_e D_e)] \sin[K_n(z_s + 2AD)] \\ &\times [(D_e v_e - Dv)(\lambda_l^2 + K_n^2) + (\mu_{ae} v_e - \mu_a v)]^{-1} \\ &\times \left\{ \exp[-(\lambda_l^2 + K_n^2) D v t - \mu_a v t] - \exp[-(\lambda_l^2 + K_n^2) D_e v_e t - \mu_{ae} v_e t] \right\}, \end{aligned} \tag{39}$$

with $a' = a + 2AD$, $s' = s + 4AD$, $K_n = n\pi/s'$, λ_l roots of $J_0(\lambda_l a') = 0$. The above equation has been obtained with the approximations $a' \cong a'_e$ and $s' \cong s'_e$. From Eq. (39) the TR reflectance can be obtained with Eq. (17) or with Eq. (19).

We stress that the presented solution can be useful to speed-up the calculations since by using Eq. (39) the computation time can be reduced of a factor ten compared to Eq. (16).

Acknowledgments

We acknowledge partial support from OILTEBIA (Optical Imaging and Laser Techniques for Biomedical Applications, ITN) under Grant 317526. The authors wish to thank Prof. Giovanni Zaccanti for his useful suggestions.